Response of the Mechanical and Chiral Character of Ethane to Ultra-Fast Laser Pulses

Xiao Peng Mi[1], Hui Lu[1], Tianlv Xu[1], Herbert Früchtl[2], Tanja van Mourik[2], Martin, J. Paterson[3], Steven R. Kirk[*1] and Samantha Jenkins[*1]

[1]Key Laboratory of Chemical Biology and Traditional Chinese Medicine Research and Key Laboratory of Resource National and Local Joint Engineering Laboratory for New Petro-chemical Materials and Fine Utilization of Resources, College of Chemistry and Chemical Engineering, Hunan Normal University, Changsha, Hunan 410081, China
[2]EaStCHEM School of Chemistry, University of Saint Andrews, North Haugh, St Andrews, Fife KY16 9ST, Scotland, United Kingdom.
[3]Institute of Chemical Sciences, School of Engineering and Physical Sciences, Heriot-Watt University, Edinburgh, EH14 4AS, UK

email: steven.kirk@cantab.net
email: samanthajsuman@gmail.com

A pair of simulated left and right circularly polarized ultra-fast laser pulses of duration 20 femtoseconds that induce a mixture of excited states are applied to ethane. The response of the electron dynamics is investigated within the next generation quantum theory of atoms in molecules (NG-QTAIM) using third-generation eigenvector-trajectories which are introduced in this work. This enables an analysis of the mechanical and chiral properties of the electron dynamics of ethane without needing to subject the C-C bond to external torsions as was the case for second-generation eigenvector-trajectories. The mechanical properties, in particular, the bond-flexing and bond-torsion were found to increase depending on the plane of the applied laser pulses. The bond-flexing and bond-torsion, depending on the plane of polarization, increases or decreases after the laser pulses are switched off. This is explainable in terms of directionally-dependent effects of the long-lasting superpositions of excited states. The chiral properties correspond to the ethane molecule being classified as formally achiral consistent with previous NG-QTAIM investigations. Future planned investigations using ultra-fast circularly polarized lasers are briefly discussed.

1. Introduction

Recently, the interdependence of steric-electronic factors was discovered to be more complex[1] than was discernable from the molecular structures for the helical electronic transitions of spiroconjugated molecules[2], [3].

Recent experiments by Beaulieu *et al.* which utilized coherent helical motion of bound electrons on neutral molecules demonstrated the need for a better understanding of the behavior of the charge density redistribution[4]. Recent advances in X-ray free-electron lasers providing ultrafast high-intensity pulses of duration 10 femtoseconds or less have allowed new experimental investigations of using non-linear effects, high-harmonic generation, and sequences of pulses with mutually-skewed polarizations to probe chiral effects and the associated electron dynamics[5]–[10]. From the theoretical standpoint, ethane was recently used to establish the next generation QTAIM (NG-QTAIM) interpretation of an achiral molecule[11]. In this earlier investigation we demonstrated that NG-QTAIM can be used to understand the staggered conformation of ethane using second-generation eigenvector trajectories[3]. We have also considered doubly halogen substituted ethane molecules and quantified their chiral character within the NG-QTAIM formalism [12].

Shaik *et al*. considered an electric field (**E**-field) as a 'smart reagent' in a range of reactions, for the control of reactivity and structure for chemical catalysis[13]. In this investigation we will use *third-generation* eigenvector trajectories within NG-QTAIM, for the first time, which are generated by an ultra-fast non-ionizing laser pulse instead of torsions that were used for the second-generation eigenvector trajectories. More specifically we will use a simulated non-ionizing ultra-fast laser pulse of 20 femtosecond duration with a peak amplitude electric-field $\pm\mathbf{E} = 200\text{x}10^{-4}$ a.u. We will consider ethane instead of ethene and a pair of right-handed (R, [+1]) and left-handed (L, [-1]) circularly polarized laser pulses. We will consider the simulated laser pulse irradiation for the three mutually orthogonal planes: *xy*, *xz* and *yz*, see **Scheme 1**.

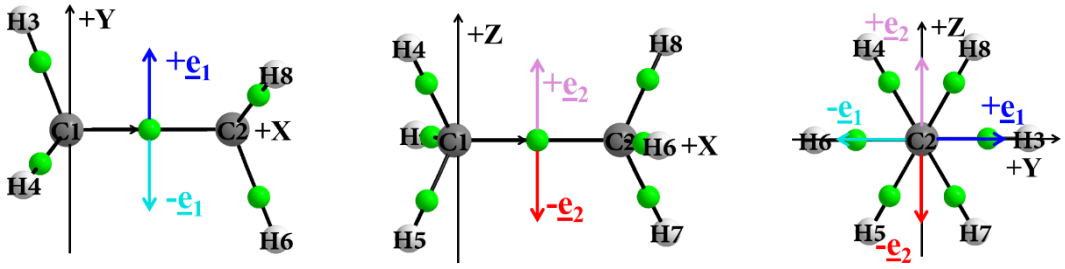

Scheme 1. The molecular graphs of ethane indicating the *xy*, *xz* and *yz* planes of the applied circularly polarized ultra-fast laser pulse are presented in the left-panel middle-panel and right-panel respectively. The most ($\pm\underline{\mathbf{e}}_2$) and least ($\pm\underline{\mathbf{e}}_1$) preferred eigenvector directions of the total charge density accumulation $\rho(\mathbf{r}_b)$ at the C1-C2 bond critical point (*BCP*) are represented by the undecorated green spheres.

Very recently, we used NG-QTAIM to quantify the effect on the electron dynamics of an ethene molecule of a simulated linearly polarized non-ionizing ultra-fast laser pulse of 20 femtosecond duration with a peak amplitude

electric-field $\pm\mathbf{E}$ = 200x10^{-4} a.u.[14]. The effects on the electron dynamics were also quantified after the laser pulse was switched off and it was discovered that the C1-C2 bond critical point (*BCP*) shifts were up to 5.8 times higher after the pulse was switched off compared with a static electric **E**-field with the same magnitude. The goals of this investigation include determining the effect of the laser pulse on the electron dynamics in terms of the mechanical properties of bond-twist, bond-flexing as well as the chiral character of left-handed counter-clockwise (CCW [-1]) and right-handed clockwise (CW [+1]) direction of an applied circularly polarized ultra-fast laser pulses, see the Theoretical Background and Computational Details sections. Additionally, we will investigate the presence of any effects on the electron dynamics in terms of the mechanical properties of bond-twist, bond-flexing as well as the chiral character remaining *after* the laser pulse is switched off and compare the effects, if any, with that present during the application of the laser pulse. Further to this we will investigate whether the effect of the laser pulse on the relative values of the chirality $\mathbb{C}$ and the bond-axiality $\mathbb{A}$ is in agreement with earlier work on ethane with second-generation eigenvector-trajectories[11]. In particular, for the first time, we will compare the effect of non-ionizing left and right circularly polarized ultra-fast laser pulses on the motion of the C1-C2 bond critical point (*BCP*). From this the C1-C2 *BCP* trajectories will be obtained with the aim of investigating if helical *BCP* trajectories will again be created as was the case using the earlier method [11] that required the imposition of geometric torsions of an exhaustive set of dihedral angles.

This earlier work proposed that the dominance of the chirality $\mathbb{C}$ over the bond-axiality $\mathbb{A}$ was evidence of the dominance of steric effects over hyper-conjugation.

2. Theoretical Background

The background of QTAIM and next generation QTAIM (NG-QTAIM)[15]–[21], which has been explained in detail in our recent tutorial review[22], is provided in the **Supplementary Materials S1**. This includes the procedure to generate the Hessian of $\rho(\mathbf{r})$ eigenvector-*following* trajectories $\mathbb{T}_{\mathbf{F}}(\boldsymbol{s})$ and the $\mathbb{U}$-space distortion set $\{\mathbb{F},\mathbb{C},\mathbb{A}\}$. Note the use of the subscript "$_{\mathbf{F}}$" to denote eigenvector-following trajectories $\mathbb{T}_{\mathbf{F}}(\boldsymbol{s})$ which are created using laser irradiation and not bond torsions as was the case for second-generation trajectories.

The ellipticity, ε, defined as $\varepsilon = |\lambda_1|/|\lambda_2| - 1$, quantifies the relative accumulation of the electronic charge density $\rho(\mathbf{r_b})$ distribution in the two directions $\pm\underline{\mathbf{e}}_1$ and $\pm\underline{\mathbf{e}}_2$ which are perpendicular to the bond-path at a Bond Critical Point (*BCP*) with position $\mathbf{r_b}$, see **Scheme 1**. For ellipticity $\varepsilon > 0$, the shortest and longest axes of the elliptical distribution of $\rho(\mathbf{r_b})$ are associated with the λ_1 and λ_2 eigenvalues, respectively. From the electron-preceding perspective a change in the electronic charge density distribution that defines a chemical bond causes in a change in atomic positions[23]. Bone and Bader later proposed that the direction of motion of the atoms that results from a slightly perturbed structure coincides with the direction of motion of the electrons[24]; this was later confirmed[25], [26].

The $\pm\underline{\mathbf{e}}_1$ and $\pm\underline{\mathbf{e}}_3$ eigenvectors lie in the *xy* plane of polarization, the $\pm\underline{\mathbf{e}}_2$ and $\pm\underline{\mathbf{e}}_3$ eigenvectors lie in the *xz* plane of polarization and the $\pm\underline{\mathbf{e}}_1$ and $\pm\underline{\mathbf{e}}_2$ eigenvectors lie in the *yz* plane of polarization, see **Scheme 1**. Note that the $\pm\mathbf{e}_2$ eigenvector corresponds to the direction in which the electrons at the *BCP* are subject to the most compressive forces[27], therefore $\pm\mathbf{e}_2$ corresponds to the most *facile*, i.e. easier, *direction* for displacement of the *BCP* electrons when the *BCP* is torsioned. Conversely the $\pm\mathbf{e}_1$ corresponds to the directions associated with the least compressive forces. The $\pm\mathbf{e}_3$ corresponds to the direction of the tensile forces on the *BCP* electrons. The bond-path is defined as the path traced out by the $\pm\underline{\mathbf{e}}_3$ eigenvector of the Hessian of the total charge density $\rho(\mathbf{r})$, passing through the *BCP*, along which $\rho(\mathbf{r})$ is locally maximal with respect to any neighboring paths.

The left and right circularly polarized laser pulses are used to create the eigenvector trajectories $\mathbb{T}(\boldsymbol{s})$ that results in a symmetry-breaking perturbation. We define the finite displacement of the *BCP* associated with a trajectory step as **dr**: note that this notation deviates from the standard use of dr as a differential and Δr as a finite difference, see also the **Supplementary Materials S1**.

The eigenvector-space trajectories $\mathbb{T}_i(\boldsymbol{s})$; $i = \{\boldsymbol{\sigma}, \rho, \mathbf{F}\}$ were constructed using the eigenvectors of the stress tensor $\boldsymbol{\sigma}(\mathbf{r})$ $\{\pm\underline{\mathbf{e}}_{1\sigma},\pm\underline{\mathbf{e}}_{2\sigma},\pm\underline{\mathbf{e}}_{3\sigma}\}$, the Hessian of $\rho(\mathbf{r})$ $\{\pm\underline{\mathbf{e}}_1,\pm\underline{\mathbf{e}}_2,\pm\underline{\mathbf{e}}_3\}$ and Ehrenfest Force $\mathbf{F}(\mathbf{r})$ Hessian $\{\pm\underline{\mathbf{e}}_{1F},\pm\underline{\mathbf{e}}_{2F},\pm\underline{\mathbf{e}}_{3F}\}$ respectively, with the corresponding reference coordinate frames defined using the eigenvectors being referred to as $\mathbb{U}_{\boldsymbol{\sigma}}$-space, $\mathbb{U}_{\rho}$-space or $\mathbb{U}_{\mathbf{F}}$-space. The reference coordinate frame is usually chosen to correspond to the minimum energy geometry. The associated trajectories, $\mathbb{T}_{\boldsymbol{\sigma}}(\boldsymbol{s})$, $\mathbb{T}_{\rho}(\boldsymbol{s})$ and $\mathbb{T}_{\mathbf{F}}(\boldsymbol{s})$, are defined as ordered sets of points with sequence parameter $\boldsymbol{s}$. For a given *BCP*, the coordinates associated with each of the points on the $\mathbb{T}_i(\boldsymbol{s})$ are calculated by evaluating the components of the shift vector $\mathbf{dr} = \mathbf{r_b}(\boldsymbol{s}) - \mathbf{r_b}(\boldsymbol{s}\text{-}1)$, $\boldsymbol{s} > 0$, where $\mathbf{r_b}$ indicates the location of the bond critical point (*BCP*), from the previous step to the current step. Every *BCP* shift vector **dr** is projected onto the eigenvectors and mapped to a *point*, e.g. for the construction of the eigenvector $\mathbb{T}(\boldsymbol{s})$: $\{(\underline{\mathbf{e}}_1\cdot\mathbf{dr}),(\underline{\mathbf{e}}_2\cdot\mathbf{dr}),(\underline{\mathbf{e}}_3\cdot\mathbf{dr})\}$ in sequence, forming the $\mathbb{T}(\boldsymbol{s})$ and similarly for the $\mathbb{T}_{\boldsymbol{\sigma}}(\boldsymbol{s})$ and $\mathbb{T}_{\mathbf{F}}(\boldsymbol{s})$. We previously published with the Hessian of $\rho(\mathbf{r})$ $\mathbb{T}(\boldsymbol{s})$ for distinguishing stereoisomers [28] and for normal modes investigations of the isotopomers of water molecules [29].

In the $\mathbb{U}$-space distortion set $\{\mathbb{F},\mathbb{C},\mathbb{A}\}$ the bond-flexing $\mathbb{F}$, defined as $\mathbb{F} = [(\mathbf{e}_1\cdot\mathbf{dr})_{max}]_{CW} - [(\mathbf{e}_1\cdot\mathbf{dr})_{max}]_{CCW}$, provides a measure of the 'flexing-strain' that a bond-path is under when subjected to an external force such as an **E**-field or a circularly polarized laser pulse.

The chirality $\mathbb{C}$ is defined as the difference in the maximum projections (the dot product of the Hessian of $\rho(\mathbf{r})$ $\mathbf{e}_2$ eigenvector and the *BCP* displacement **dr**) of the $\mathbb{T}_{\mathbf{F}}(\boldsymbol{s})$ values between the left-handed circularly polarized (L, CCW [-1]) and right-handed (R, CCW [+1]) circularly polarized laser pulse: $\mathbb{C} = [(\mathbf{e}_2\cdot\mathbf{dr})_{max}]_{CW} - [(\mathbf{e}_2\cdot\mathbf{dr})_{max}]_{CCW}$.

The chirality $\mathbb{C}$ quantifies the *circular* displacement of the C1-C2 *BCP* i.e., where the largest magnitude Hessian

of $\rho(\mathbf{r})$ eigenvalue (λ_2) is associated with $\pm\mathbf{e}_2$. The $\pm\mathbf{e}_2$ corresponds to the direction in which the electrons at the *BCP* will be most easily displaced when the *BCP* is subjected to circular displacement i.e. torsion[27]. The signs of the chirality $\mathbb{C}$ and bond-axiality $\mathbb{A}$ determine the dominance of **S** ($\mathbb{C} > 0$, $\mathbb{A} > 0$) or **R** ($\mathbb{C} < 0$, $\mathbb{A} < 0$) character, see **Table 3**. The intermediate results for the $\mathbb{U}$-space distortion sets are provided in the **Supplementary Materials S7**.

The bond-axiality $\mathbb{A}$, which provides a measure of the chiral asymmetry, is defined as $\mathbb{A} = [(\mathbf{e}_3 \cdot \mathbf{dr})_{max}]_{CW} - [(\mathbf{e}_3 \cdot \mathbf{dr})_{max}]_{CCW}$**.** This quantifies the direction of *axial* displacement of the bond critical point (*BCP*) in response to the left-handed (CCW [-1]) and right-handed (CW [+1]) circularly polarized laser pulses, i.e. the sliding of the *BCP* along the bond-path[29]. The chirality-helicity function $\mathbb{C}_{helicity} = \mathbb{C}|\mathbb{A}|$, i.e., the numerical product of the chirality and the magnitude of the bond-axiality $\mathbb{A}$, which can be used to determine the nature of any chiral behaviors present in ethane in the absence or presence of a circularly polarized laser pulse. The chirality-helicity function $\mathbb{C}_{helicity}$ will only be used for the *yz* plane of polarization.

A null-chirality assignment **Q**, defined for values of $\mathbb{C}_{helicity} \approx 0$ was previously discovered for ethane using second-generation eigenvector trajectories[3]. The choice of (±) sign is therefore not used with the chirality assignment **Q** as it is for the **S** and **R** assignments.

Note, we previously thoroughly investigated the chirality helicity function $\mathbb{C}_{helicity}$ for chiral molecules which included an investigation on the chiral doubly halogen (F,Cl), (Cl,Br) and (Br,F) substituted ethane molecules [12]. We found in each of these three cases the $\mathbb{C}_{helicity}$ was significant, i.e. non-zero. Values of the $\mathbb{C}_{helicity}$ for the S structural stereoisomers correspond to +0.034, +0.124 and +0.043 for the (F,Cl), (Cl,Br) and (Br,F) substituted ethane molecules respectively. The values for the R structural stereoisomers were found to be -0.034, -0.124 and -0.043. Notice the sign difference +/- in the $\mathbb{C}_{helicity}$ values of the S and R stereoisomers.

In this investigation we will use the $\mathbb{U}$-space distortion set $\{\mathbb{F},\mathbb{T},\mathbb{A}\}$ for the *xy* and *xz* planes of the applied circularly polarized ultra-fast laser pulse, and the $\mathbb{U}$-space distortion set $\{\mathbb{F},\mathbb{C},\mathbb{A}\}$ for the *yz* plane, i.e. the bond twist $\mathbb{T}$ has the same definition as the chirality $\mathbb{C}$ but is used in situations not appropriate for chirality such as investigations of the *cis*-effect[30]. As a consequence in this investigation we introduce the twist-helicity $\mathbb{T}_{helicity} = \mathbb{T}|\mathbb{A}|$, i.e., the numerical product of the bond-twist and the magnitude of the bond-axiality $\mathbb{A}$, can be used to determine the nature of any bond-twist and bond-flexing, i.e. mechanical distortions present in ethane as a response to the presence of a circularly polarized laser pulse. The twist-helicity function $\mathbb{T}_{helicity}$ will be used for the *xy* and *xz* planes of polarization.

3. Computational Details

The geometry of the ethane molecule was first optimized in zero applied external electric field and pseudo-CI (configuration interaction) singles eigenvectors were then built using a set of configuration state functions in the zero external electric (**E**) field case, using the hybrid linear response time-dependent density functional theory/configuration interaction (LR-TDDFT/CI) approach described in detail in previous work[31]–[33]. This was carried out using LR-TDDFT at the CAM-B3LYP[34]/aug-cc-pVTZ[35], [36] level. Both this choice of functional and this basis set have been shown elsewhere in the literature[37] to provide accurate descriptions of excited states. The fifty lowest-energy excited states were computed using the Gaussian G09 v.E.01[38] package using an 'ultrafine' integration grid and no symmetry constraints. A linear combination of singly-excited configuration state functions was used to construct each time-independent many-electron state. Using the time-dependent CI implementation as implemented in the detCI module[31], [32] within the ORBKIT[39] package, a 'library' of transition dipole moments between states was precomputed for later use. The electron dynamics were then propagated within the 'clamped nuclei' approximation, with the wavefunction being propagated as a linear complex-weighted sum of the previously computed pseudo-CI singles states, as described in previous work[31], [32].

It is possible to model the physical effect of the laser pulse driving out-of-equilibrium polarization in the electron density using a number of methods, including the 'real-time TD-DFT', aka 'time-dependent Kohn-Sham', methods of Zhu *et al*. [40], [41]. The alternative used in this work, the hybrid (TD-DFT/TDCI) approach previously described by Tremblay *et al*. [42], [43] takes the necessary account of state-mixing and has the advantage of being able to use the CI-singles states, energies and transition dipole moments computed by any quantum chemistry code. In this approach, the field-free Hamiltonian is used, along with the additional semi-classical dipole interaction approximation term $-\boldsymbol{\mu}.\mathbf{E}(t)$, where the dot indicates a vector dot product, $\boldsymbol{\mu}$ is the dipole operator and $\mathbf{E}(t)$ is the time-dependent applied electric field vector, with dipoles being evaluated using the aforementioned transition densities.

The pre-computed dipole moment library was used at each dynamics time-step to calculate the dipole interaction term $-\boldsymbol{\mu}.\mathbf{E}(t)$ and the electron dynamics were propagated for a total of 100 fs in the 'interaction' representation.

Commencing at the start of the electron dynamics calculation t = 0 fs, a time-dependent electric field vector $\mathbf{E}(t)$ was applied in the form of a single 20 fs duration 'sine-squared'-shaped circularly-polarized laser pulse of peak amplitude $200\text{x}10^{-4}$ a.u. To simulate a circularly polarized pulse, three mutually orthogonal polarization planes were first defined with electric field components $[\mathbf{E}_{\boldsymbol{n}}(t), \mathbf{E}_{\boldsymbol{m}}(t)]$ in each polarization plane, where $(\boldsymbol{n},\boldsymbol{m}) = (x,y)$, (x,z) and (y,z), with x,y and z corresponding to the molecular coordinate axes defined earlier. The overall field vector $[\mathbf{E}_{\boldsymbol{n}}(t), \mathbf{E}_{\boldsymbol{m}}(t)]$ was computed by multiplying together three terms:

1. The 'carrier' wave, commencing at time t = 0 fs with initial phase = 0, taken as the vector $[\sin(\omega t) , \sin(\omega t + \pi/2)]$ in the $(\boldsymbol{n},\boldsymbol{m})$ polarization plane, with ω being the selected laser excitation frequency.

2. The 'amplitude envelope' of a single pulse as a half-cycle 'sine-squared'-shaped function $E_{peak} \sin^2(\omega_{env}t)$, also commencing at time $t = 0$ with phase = 0, of peak field amplitude $E_{peak} = 200\text{x}10^{-4}$ a.u., with ω_{env} selected to give a half-cycle, i.e., yielding a single pulse, time of 20 fs.

3. A polarization factor of +1 or -1, applied only to the $\mathbf{E}_{\boldsymbol{m}}(t)$ field component: this choice yielded a resultant electric field vector which turned either clockwise [CW, +1] or counterclockwise [CCW,-1] in the (***n***,***m***) polarization plane with increasing time *t*, see **Scheme S2** in **Supplementary Materials S2**.

The electric field **E** components as a function of time were precomputed and tabulated at 2313 equally-spaced times from $t = 0$ fs to $t = 20$ fs. The time-dependent CI dynamics calculation then computed the instantaneous field at any given dynamics timestep by cubic-spline interpolation from these precomputed values.

A 'field broadening' approach was employed: for a '$\sin^2$' amplitude envelope function pulse of duration ΔT the energetic broadening of the field is simply $\Delta E = \hbar/\Delta T$. Low-lying electronic states are usually well separated energetically, so only very short pulses, such as the 20 fs pulse used here, are broad enough to excite the desired superposition states. As short pulses are inherently energetically broad, they are also inevitably unselective.

Therefore a laser carrier frequency (excitation energy) of $\omega = 0.350$ a.u. was chosen to induce a superposition of lower-lying excited states, see the **Supplementary Materials S2** and **S3**. More selective strategies for excitation of superposition states are still being actively sought in the research literature, e.g. 'undertuning' and 'overtuning' strategies have had only partial success [44], although laser-induced selective alignment of molecules relative to fields is now experimentally feasible [45], [46].

The electron dynamics was propagated using a dynamics timestep of $8.6388\text{x}10^{-4}$ fs, chosen to yield exactly 80 dynamics timesteps per cycle of the chosen laser carrier frequency (excitation energy) $\omega = 0.350$ a.u. Populations describing the content of the superposition state were recorded every 20 dynamics timesteps. These were confirmed to preserve overall normalization during the entire dynamics simulation. The total charge density distribution $\rho(\mathbf{r})$ was constructed from the first-order reduced density matrix (1RDM) and dumped to disk storage every 5 dynamics timesteps. At each of these 1RDM timesteps, a snapshot of the total electronic charge density distribution $\rho(\mathbf{r})$ was generated as a 'gridded' scalar field with a grid spacing of 0.1 a.u. and a grid edge padding distance of 4.0 a.u. on all sides of the molecule.

A number of 'timeslices' were defined within the dynamics run, each corresponding to two full cycles of the laser excitation frequency (equating to 201 1RDM steps), centered on $t = 5$, 10 and15 fs i.e., during the laser pulse and $t = 40$, 60, 80 fs, after the laser pulse. The CRITIC2 code[47] with the 'density-smoothing'[48] option was used to obtain the bond critical points (*BCP*s), bond paths and eigenvectors of the Hessian of the density $\rho(\mathbf{r})$ for each snapshot, ensuring that the Poincaré-Hopf relationship was satisfied in all cases. NG-QTAIM properties were obtained using the in-house QuantVec[49] suite which is compatible with the CRITIC2 code. Eigenvector-following NG-QTAIM trajectories were then calculated for each 'timeslice'.

4. Results and discussions

The tabulated excitation frequencies are provided in the **Supplementary Materials S2** and the populations for a carrier excitation frequency ω = 0.350 a.u. for the planes of circular laser pulse polarization *xy*, *xz* and *yz* are provided in the **Supplementary Materials S3-S5** respectively. Each selected time slice corresponds to two full cycles of the carrier excitation frequency ω.

The variations of the ethane C1-C2 *BCP* ellipticity ε for the right-handed (**CW, [+1]**) and left-handed (**CCW, [-1]**) circularly polarized laser pulse in the *xy, xz* and *yz* planes, for a selection of times for the duration of the laser pulse and after it is switched off, are provided in **Figures S6(I-III)** respectively of the **Supplementary Materials S6**, also see **Scheme 1**.

There are significant differences in both the amplitude and symmetry of the C1-C2 *BCP* ellipticity ε in response to the right-handed (**CW, [+1]**) and left-handed (**CCW, [-1]**) circularly polarized laser pulse corresponding to the *xy* plane, see **Figure S6(I)**. This is simply due to the lower symmetry of the ethane molecule in the *xy* plane compared with the *xz* and *yz* planes, see **Scheme 1**. At around 5 fs the variation for the *xy* plane is approximately periodic with an interval of 0.2 fs, although this trend weakens for later times.

The responses as determined by the variation of the ellipticity ε for both the right-handed (**CW, [+1]**) and left-handed (**CCW, [-1]**) circularly polarized laser pulse polarized in *xz* plane are rather similar to each other and both follow regular sinusoidal type variations at intervals of approximately 0.2 fs, see **Figure S6(II)**. The corresponding variations, again approximately 0.2 fs for the *xz* plane are similar to each and are vary with a regular periodicity but are not sinusoidal, see **Figure S6(III)**.

The C1-C2 *BCP* ellipticity ε does not provide a complete understanding of the response of the electron charge density distribution $\rho(\mathbf{r_b})$ at the C1-C2 *BCP* to the circularly polarized laser pulse, due to the lack of full symmetry-breaking[50] as a result of the lack of consideration of the $\pm\underline{\mathbf{e}}_1$, $\pm\underline{\mathbf{e}}_2$ and $\pm\underline{\mathbf{e}}_3$ eigenvectors. To overcome this limitation the eigenvector-following trajectories $\mathbb{T}_F(s)$ will be used, see **Tables 1-3** and **Figures 1-3**. Only the laser pulses (**CW, [+1]**) (**CCW, [-1]**) in the *xy* plane possess significant values of the twist-helicity $\mathbb{T}_{helicity}$ or chirality-helicity $\mathbb{C}_{helicity}$, see **Figure 1** and **Tables 1-3**. The corresponding laser pulses in the *xz* and *yz* planes possess either zero or negligible values of the twist-helicity $\mathbb{T}_{helicity}$ or chirality-helicity $\mathbb{C}_{helicity}$, both for the duration and after the pulse is switched off, see **Table 2** and **Table 3** respectively. The corresponding values of the bond-axiality $\mathbb{A}$, which comprise the twist-helicity $\mathbb{T}_{helicity} = \mathbb{T}|\mathbb{A}|$ or chirality-helicity $\mathbb{C}_{helicity} = \mathbb{C}|\mathbb{A}|$, are insignificant for both corresponding laser pulses in the *xz* and *yz* planes.

Larger values of the $\mathbb{U}$-space distortion set $\{\mathbb{F},\mathbb{T},\mathbb{A}\}$ for the *xy* and *xz* planes of the applied circularly polarized ultra-fast laser pulse are present after the pulse duration than during the pulse, see **Figure 2**, **Table 1** and **Figure 3** and **Table 2**. The eigenvector-following trajectories $\mathbb{T}_F(s)$ for the (**CW, [+1]**) and (**CCW, [-1]**) in response to

the laser pulses are distinguishable for each of the *xy*, *xz* and *yz* planes of polarization for the pulse duration and after the pulse is switched-off. This is apparent from the clear separation of the (**CW, [+1]**) and (**CCW, [-1]**) $\mathbb{T}_{\mathbf{F}}(\boldsymbol{s})$ indicated by the red and blue tracks in **Figures 1-3** respectively.

After the pulse is switched off in the *xy* and *xz* planes of polarization the response to the laser pulses in terms of the mechanical properties, bond-flexing $\mathbb{F}$ and bond-twist $\mathbb{T}$, increases in some cases. For polarization in the *yz* plane the response to the laser attenuated in the form of smaller values of the $\mathbb{U}$-space distortion set $\{\mathbb{F},\mathbb{C},\mathbb{A}\}$ for the *yz* plane of polarization. The helical-shaped trajectories $\mathbb{T}_{\mathbf{F}}(\boldsymbol{s})$ are most apparent, in all cases, after the pulse is switched off, see sub-figures **(e-g)** of **Figures 1-3**.

The magnitudes of the bond-flexing $\mathbb{F}$ are greater than those of the bond-twist $\mathbb{T}$ in all cases for the polarization in the *xy* plane for the duration of the pulse but not after the pulse. The bond-twist $\mathbb{T}$ dominates the bond-flexing $\mathbb{F}$ for the duration of the pulse for polarization in the *xz* plane, see **Table 1** and **Table 2** respectively. In contrast the values of the $\mathbb{U}$-space distortion set $\{\mathbb{F},\mathbb{T},\mathbb{A}\}$ for the *yz* plane are lower after the duration of the pulse than during the pulse, see **Figure 3** and **Table 3**.

Table 1. The C1-C2 *BCP* $\mathbb{U}$-space distortion sets $\mathbb{F}$ = bond-flexing, $\mathbb{T}$ = bond-twist and $\mathbb{A}$ = bond-axiality in the presence of an applied circularly polarized ultra-fast laser pulse in the *xy* plane. The twist-helicity function $\mathbb{T}_{helicity} = \mathbb{T}x|\mathbb{A}|$.

	$\{\mathbb{F}, \mathbb{T}, \mathbb{A}\}$	$\mathbb{T}_{helicity}$
During laser pulse		
$t = 5$	{ 0.013967, 0.027852, -0.011976}	0.000334
$t = 10$	{-0.265463, 0.264775, -0.009513}	0.002519
$t = 15$	{-0.318884, 0.169852, -0.260291}	0.044211
After laser pulse		
$t = 40$	{-0.081207, 0.168731, -0.229059}	0.038649
$t = 60$	{ 0.005205, -0.029962, -0.170584}	-0.005111
$t = 80$	{-0.419727, 0.260627, -0.217924}	0.056797

Table 2. The C1-C2 *BCP* $\mathbb{U}$-space distortion sets $\{\mathbb{F}, \mathbb{T}, \mathbb{A}\}$ in the presence of an applied *xz* plane of the applied circularly polarized ultra-fast laser pulse of the applied circularly polarized ultra-fast laser pulse. The value of the $\mathbb{T}_{helicity} = 0$ for the duration of the laser pulse, see the caption of **Table 1** for further details.

	$\{\mathbb{F}, \mathbb{T}, \mathbb{A}\}$	$\mathbb{T}_{helicity}$
During laser pulse		
$t = 5$	{ 0.015550, -0.074544, -0.000006}	0.000000
$t = 10$	{ 0.000377, -0.000511, -0.000037}	0.000000
$t = 15$	{-0.000846, 0.000895, 0.000031}	0.000000

After laser pulse		
$t = 40$	{-0.002994, 0.016536, 0.000084}	0.000001
$t = 60$	{ 0.022848, -0.021906, 0.000042}	-0.000001
$t = 80$	{ 0.020022, -0.036828, 0.000045}	-0.000002

Table 3. The C1-C2 *BCP* $\mathbb{U}$-space distortion sets $\{\mathbb{F}, \mathbb{C}, \mathbb{A}\}$ and the chirality-helicity function $\mathbb{C}_{helicity} = \mathbb{C}x|\mathbb{A}|$ in the presence of an applied circularly polarized ultra-fast laser pulse in the *yz* plane. The value of the chirality-helicity function $\mathbb{C}_{helicity} = 0$ in all cases.

	$\{\mathbb{F}, \mathbb{C}, \mathbb{A}\}$
During laser pulse	
$t = 5$	{-0.012998, 0.003554, 0.000009}
$t = 10$	{ 0.009309, 0.007960, -0.000025}
$t = 15$	{-0.002108, -0.002168, 0.000039}
After laser pulse	
$t = 40$	{0.000306, 0.000859, 0.000005}
$t = 60$	{0.000550, -0.000429, 0.000092}
$t = 80$	{0.001990, -0.001217, -0.000046}

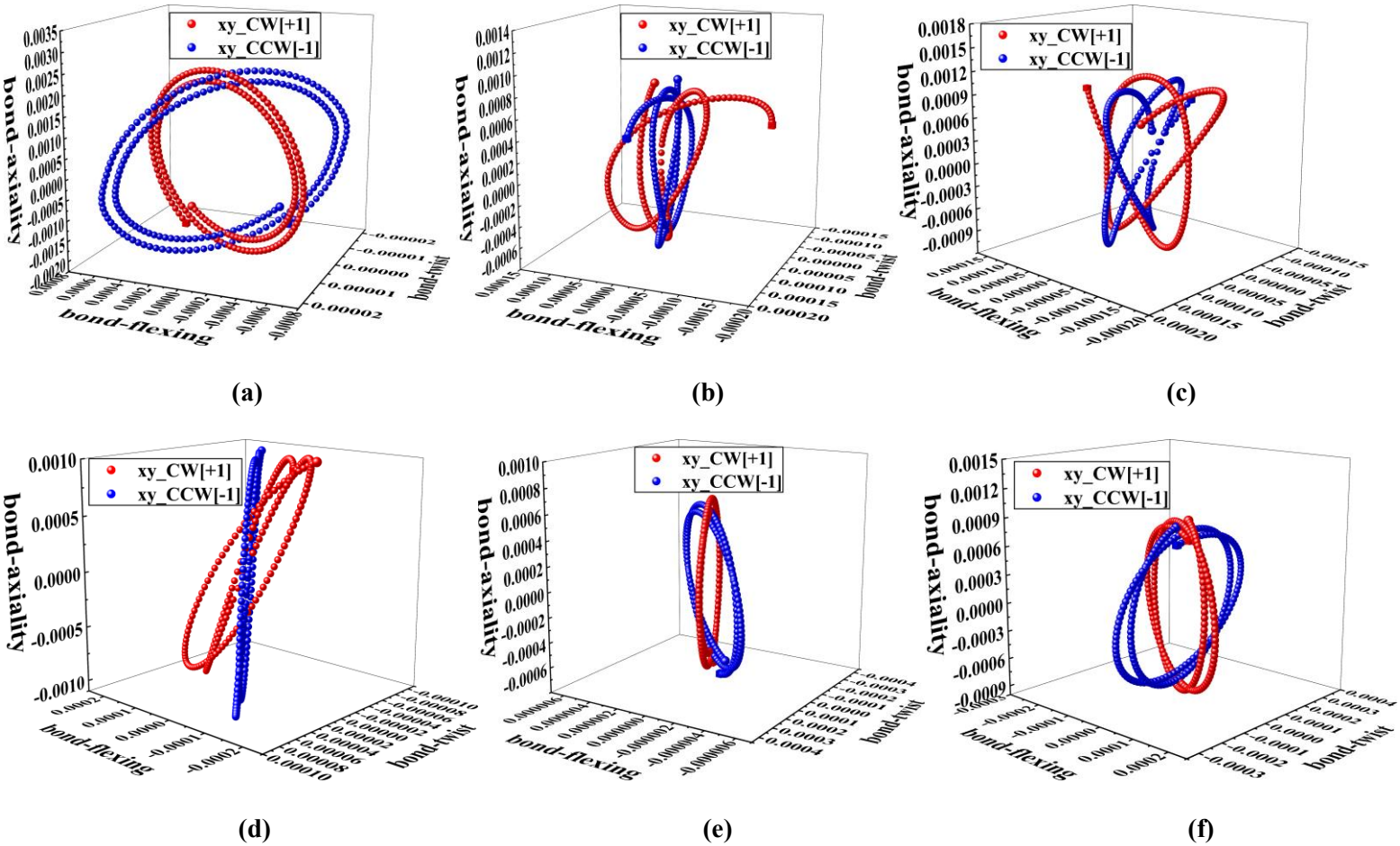

Figure 1. The ethane C1-C2 *BCP* Hessian of $\rho(\mathbf{r})$ eigenvector trajectories $\mathbb{T}(s)$ for the for the right-handed, clockwise (*R*, [+1]) and left-handed, counter-clockwise (*L*, [-1]) circularly polarized laser pulses in the *xy* plane during the pulse at $t = 5$ femtoseconds (fs), $t = 10$ fs, $t = 15$ fs are presented in sub-figures **(a-c)** respectively. The corresponding plots after the pulse is switched off are presented at $t = 40$ fs, $t = 60$ fs and $t = 80$ fs in sub-figures **(d-f)** respectively.

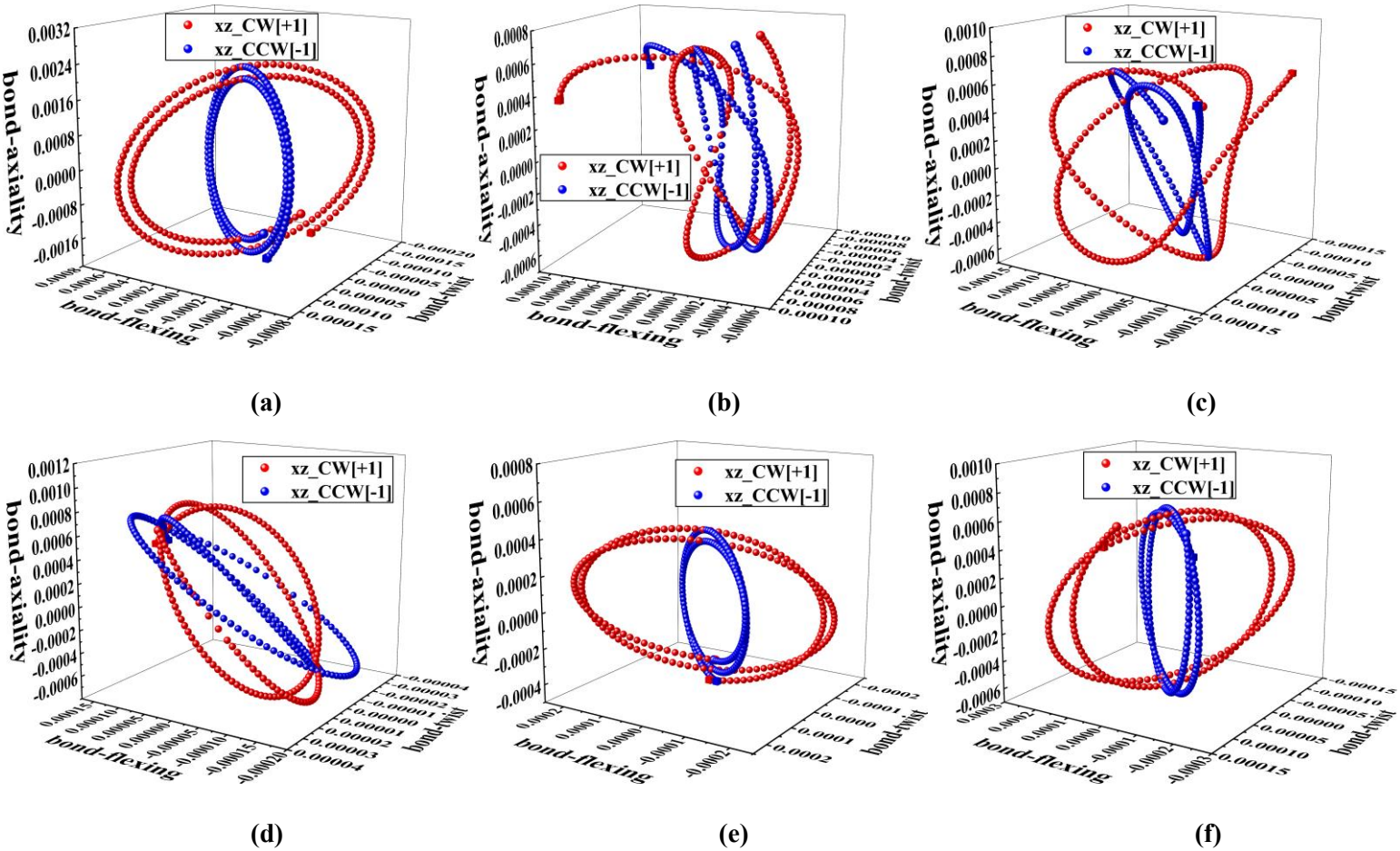

Figure 2. The ethane C1-C2 *BCP* $\mathbb{T}(s)$ for the for the (CW, [+1]) and (CCW, [-1]) circularly polarized laser pulses in the *xz* plane during the pulse at t = 5 femtoseconds (fs), t =10 fs, t = 15 fs are presented in sub-figures **(a-c)** respectively. The corresponding plots after the pulse is switched off are presented at t = 40 fs, t = 60 fs and t = 80 fs in sub-figures **(d-f)** respectively, see the caption of **Figure 1** for further details.

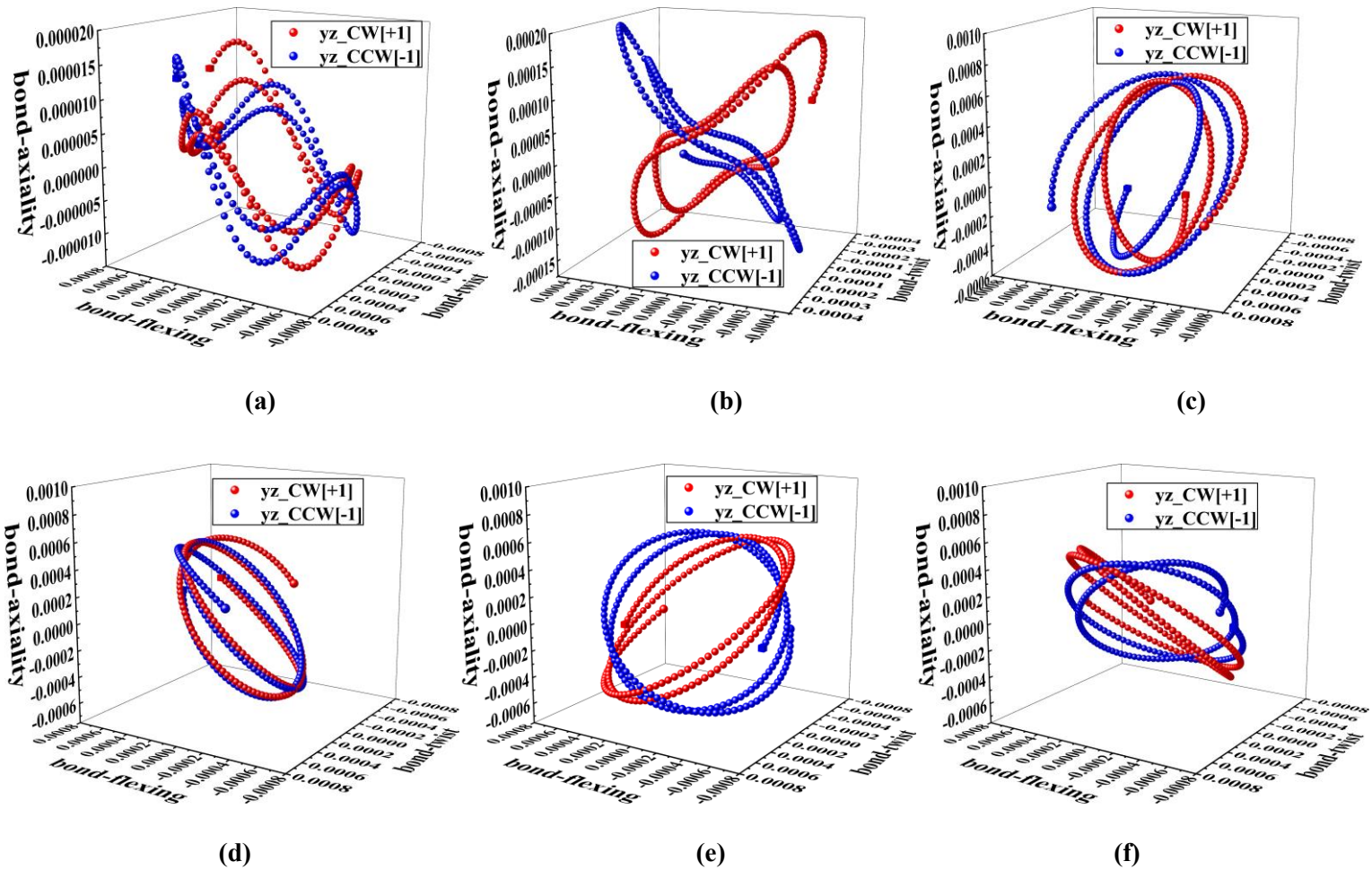

Figure 3. The ethane C1-C2 *BCP* $\mathbb{T}(s)$ for the for the (CW, [+1]) and (CCW, [-1]) circularly polarized laser pulses in the *yz* plane during the pulse at t = 5 femtoseconds (fs), t =10 fs, t = 15 fs are presented in sub-figures **(a-c)** respectively. The corresponding plots after the pulse is switched off are presented at t = 40 fs, t = 60 fs and t = 80 fs in sub-figures **(d-f)** respectively, see the caption of **Figure 1** for further details.

For polarization in the *yz* plane there is no dominance in the magnitudes of the bond-flexing $\mathbb{F}$ values compared with the those of the chirality $\mathbb{C}$, see **Table 3**.

5. Conclusions

In this investigation we have used NG-QTAIM to quantify changes to the mechanical and chiral properties, associated with the electron dynamics of ultra-fast non-ionizing circularly polarized laser pulses of duration 20 femtoseconds that induced a mixture of excited states. NG-QTAIM was demonstrated to distinguish the response of the C1-C2 *BCP* to the left-handed circularly polarized (L, CCW [-1]) and right-handed (R, CW [+1]) circularly polarized laser pulses in all cases. This was apparent from the corresponding non-overlapping eigenvector trajectories $\mathbb{T}(s)$ which demonstrated the utility of the vector-based approach. The timeslice used was

demonstrated to be sufficient to result in a 4π rotation of the C1-C2 *BCP*, evident from the two complete revolutions of the $\mathbb{T}(s)$ in all cases. This demonstrates that the response of the simulated laser irradiation as determined with NG-QTAIM was sufficient to determine the mechanical and chiral properties without requiring any geometric torsions. We first quantified the response of the electron dynamics to the circularly polarized laser pulses of the scalar C1-C2 *BCP* ellipticity ε. We found a significant response of the C1-C2 *BCP* ellipticity ε in all three planes of polarization: *xy*, *xz* and *yz*, both during and after the application of the laser pulses. The largest response of the C1-C2 *BCP* ellipticity ε was found for the *xy* plane of polarization. This is consistent with the fact that the *xy* plane of polarization includes the $\pm\underline{\mathbf{e}}_1$ eigenvector that corresponds to the largest negative eigenvalue λ_1 of the Hessian of $\rho(\mathbf{r})$. This demonstrates that the chosen laser pulses are sufficient to induce a significant response in the electron dynamics despite a complete absence of nuclear motion.

Quantification of the response of the mechanical properties, bond-flexing $\mathbb{F}$ and bond-torsion $\mathbb{T}$ to the laser pulses was undertaken with the third-generation eigenvector-following trajectories $\mathbb{T}_{\mathbf{F}}(\boldsymbol{s})$ using the $\mathbb{U}$-space distortion set $\{\mathbb{F},\mathbb{T},\mathbb{A}\}$ for the *xy* and *xz* planes of polarization. For the *xy* plane of polarization, the bond-flexing $\mathbb{F}$ was found to increase with time for the duration of the pulse. This is explained by the fact that the *xy* plane contains the $\pm\underline{\mathbf{e}}_1$ eigenvector (least preferred direction of $\rho(\mathbf{r}_b)$ accumulation) which is used to quantify the bond-flexing $\mathbb{F}$ in the trajectory $\mathbb{T}_{\mathbf{F}}(\boldsymbol{s})$ plots. The application of the laser pulses in the *xz* plane, which contains the $\pm\underline{\mathbf{e}}_2$ eigenvector (most preferred direction of $\rho(\mathbf{r}_b)$ accumulation), resulted in larger magnitudes of the bond-twist $\mathbb{T}$ than the bond-flexing $\mathbb{F}$ for a given time. This is explainable by the fact that the $\pm\underline{\mathbf{e}}_2$ eigenvector is used to quantify the bond-twist $\mathbb{T}$.

The increased response after laser pulses in the *xy* plane of polarization are switched off is consistent with our recent work where linearly polarized ultra-fast lasers were applied to an ethene molecule[14]. For the *xz* plane however values of the $\mathbb{T}_{helicity} = 0$ during the pulse and insignificant after the pulse was switched off due to extremely low values of the bond-axiality $\mathbb{A}$.

Third generation $\mathbb{T}(\boldsymbol{s})$ with the $\mathbb{U}$-space distortion set $\{\mathbb{F},\mathbb{C},\mathbb{A}\}$ revealed and quantified the chiral character in response to the laser pulses for the *yz* plane of polarization. The chiral character was determined from the value of the chirality-helicity function $\mathbb{C}_{helicity} = 0$ for all times during and after the application of the laser pulses and is consistent with the expectations for an achiral molecule. The presence of larger values of bond-flexing $\mathbb{F}$ and bond-torsion $\mathbb{T}$ after the pulses are switched off for the *xy* and *xz* but lower values for the *yz* planes of polarization can be explained in terms of the effects of directionally dependent long-lasting superposition of excited states on $\rho(\mathbf{r}_b)$.

In all cases both during and after the application of the laser pulses, the value of the chirality $\mathbb{C}$ dominates the bond-axiality $\mathbb{A}$ in agreement with earlier work on ethane with second-generation eigenvector-trajectories. This again demonstrates, within NG-QTAIM, the dominance of steric effects ($\mathbb{C}$) over hyperconjugation ($\mathbb{A}$) in ethane. Future planned work includes consideration of chiral molecules, including singly and doubly halogen substituted ethane to understand how ultra-fast lasers may influence chiral character and also (mixed) achiral character[12]. In addition, the laser carrier envelope phase difference will be varied to induce different time dependent mixtures of excited states.

Conflict of Interests Statement

The authors have no conflict of interests to declare.

Funding Information

The Hunan Natural Science Foundation of China project gratefully acknowledged approval number: 2022JJ30029. The One Hundred Talents Foundation of Hunan Province is also gratefully acknowledged for the support of S.J. and S.R.K. H.F. and T.v.M. gratefully acknowledge computational support via the EaStCHEM Research Computing Facility. We also would like to thank our sponsor Paul Ayers for provision access to SHARCnet Compute Canada supercomputing facilities.

References

[1] K. C. Harper, M. S. Sigman, *Science*, **2011**, DOI:10.1126/science.1206997.
[2] M. H. Garner, C. Corminboeuf, *Chem. Commun.*, **2021**, DOI:10.1039/D1CC01904J.
[3] H. Xing, A. Azizi, R. Momen, T. Xu, S. R. Kirk, S. Jenkins, *Int. J. Quantum Chem.*, **2022**, DOI:10.1002/qua.26884.
[4] S. Beaulieu, A. Comby, D. Descamps, B. Fabre, G. A. Garcia, R. Géneaux, A. G. Harvey, F. Légaré, Z. Mašín, L. Nahon, A. F. Ordonez, S. Petit, B. Pons, Y. Mairesse, O. Smirnova, V. Blanchet, *Nature Phys*, **2018**, DOI:10.1038/s41567-017-0038-z.
[5] R. Cireasa, A. E. Boguslavskiy, B. Pons, M. C. H. Wong, D. Descamps, S. Petit, H. Ruf, N. Thiré, A. Ferré, J. Suarez, J. Higuet, B. E. Schmidt, A. F. Alharbi, F. Légaré, V. Blanchet, B. Fabre, S. Patchkovskii, O. Smirnova, Y. Mairesse, V. R. Bhardwaj, *Nature Phys*, **2015**, DOI:10.1038/nphys3369.
[6] A. Yachmenev, S. N. Yurchenko, *Phys. Rev. Lett.*, **2016**, DOI:10.1103/PhysRevLett.117.033001.
[7] Y. Harada, E. Haraguchi, K. Kaneshima, T. Sekikawa, *Phys. Rev. A*, **2018**, DOI:10.1103/PhysRevA.98.021401.
[8] D. Baykusheva, D. Zindel, V. Svoboda, E. Bommeli, M. Ochsner, A. Tehlar, H. J. Wörner, *Proceedings of the National Academy of Sciences*, **2019**, DOI:10.1073/pnas.1907189116.
[9] O. Neufeld, D. Ayuso, P. Decleva, M. Y. Ivanov, O. Smirnova, O. Cohen, *Phys. Rev. X*, **2019**, DOI:10.1103/PhysRevX.9.031002.
[10] J. Vogwell, L. Rego, O. Smirnova, D. Ayuso, *Science Advances*, **2023**, DOI:10.1126/sciadv.adj1429.
[11] Z. Li, T. Xu, H. Früchtl, T. van Mourik, S. R. Kirk, S. Jenkins, *Chem. Phys. Lett.*, **2022**, DOI:10.1016/j.cplett.2022.139669.
[12] Z. Li, T. Xu, H. Früchtl, T. van Mourik, S. R. Kirk, S. Jenkins, *Chem. Phys. Lett.*, **2022**, DOI:10.1016/j.cplett.2022.139762.

[13] S. Shaik, D. Danovich, J. Joy, Z. Wang, T. Stuyver, *J. Am. Chem. Soc.*, **2020**, DOI:10.1021/jacs.0c05128.
[14] H. Lu, A. Azizi, X. Mi, W. Yu, Y. Peng, T. Xu, H. Früchtl, T. van Mourik, S. R. Kirk, S. Jenkins, *Journal of Computational Chemistry*, **2023**, DOI:10.1002/jcc.27126.
[15] M. X. Hu, T. Xu, R. Momen, A. Azizi, S. R. Kirk, S. Jenkins, *Chem. Phys. Lett.*, **2017**, DOI:10.1016/j.cplett.2017.04.017.
[16] W. J. Huang, T. Xu, S. R. Kirk, M. Filatov, S. Jenkins, *Chem. Phys. Lett.*, **2018**, DOI:10.1016/j.cplett.2018.10.029.
[17] J. H. Li, W. J. Huang, T. Xu, S. R. Kirk, S. Jenkins, *Int. J. Quantum Chem.*, **2018**, DOI:10.1002/qua.25847.
[18] H. Guo, A. Morales-Bayuelo, T. Xu, R. Momen, L. Wang, P. Yang, S. R. Kirk, S. Jenkins, *J. Comput. Chem.*, **2016**, DOI:10.1002/jcc.24499.
[19] P. Yang, T. Xu, R. Momen, A. Azizi, S. R. Kirk, S. Jenkins, *Int. J. Quantum Chem.*, **2018**, DOI:10.1002/qua.25565.
[20] T. Xu, L. Wang, Y. Ping, T. van Mourik, H. Früchtl, S. R. Kirk, S. Jenkins, *Int. J. Quantum Chem.*, **2018**, DOI:10.1002/qua.25676.
[21] T. Xu, J. Farrell, R. Momen, A. Azizi, S. R. Kirk, S. Jenkins, D. J. Wales, *Chem. Phys. Lett.*, **2017**, DOI:10.1016/j.cplett.2016.11.028.
[22] S. R. Kirk, S. Jenkins, *Chem. Soc. Rev.*, **2023**, DOI:10.1039/D3CS00350G.
[23] H. Nakatsuji, *J. Am. Chem. Soc.*, **1974**, DOI:10.1021/ja00808a004.
[24] R. G. A. Bone, R. F. W. Bader, *J. Phys. Chem.*, **1996**, DOI:10.1021/jp953512m.
[25] S. Jenkins, M. I. Heggie, *J. Phys.: Condens. Matter*, **2000**, DOI:10.1088/0953-8984/12/49/3.
[26] P. W. Ayers, S. Jenkins, *J. Chem. Phys.*, **2009**, DOI:10.1063/1.3098140.
[27] P. Szarek, Y. Sueda, A. Tachibana, *J. Chem. Phys.*, **2008**, DOI:10.1063/1.2973634.
[28] T. Xu, S. R. Kirk, S. Jenkins, *Chem. Phys. Lett.*, **2020**, DOI:10.1016/j.cplett.2019.136907.
[29] T. Tian, T. Xu, S. R. Kirk, I. T. Rongde, Y. B. Tan, S. Manzhos, Y. Shigeta, S. Jenkins, *Phys. Chem. Chem. Phys.*, **2020**, DOI:10.1039/C9CP05879F.
[30] Y. Peng, W. Yu, X. Feng, T. Xu, H. Früchtl, T. van Mourik, S. R. Kirk, S. Jenkins, *Molecules*, **2022**, DOI:10.3390/molecules27186099.
[31] V. Pohl, G. Hermann, J. C. Tremblay, *Journal of Computational Chemistry*, **2017**, DOI:10.1002/jcc.24792.
[32] G. Hermann, V. Pohl, J. C. Tremblay, *Journal of Computational Chemistry*, **2017**, DOI:10.1002/jcc.24896.
[33] S. Giri, A. M. Dudzinski, J. C. Tremblay, G. Dixit, *Phys. Rev. A*, **2020**, DOI:10.1103/PhysRevA.102.063103.
[34] T. Yanai, D. P. Tew, N. C. Handy, *Chemical Physics Letters*, **2004**, DOI:10.1016/j.cplett.2004.06.011.
[35] R. A. Kendall, T. H. Dunning, R. J. Harrison, *J. Chem. Phys.*, **1992**, DOI:10.1063/1.462569.
[36] T. H. Dunning, *J. Chem. Phys.*, **1989**, DOI:10.1063/1.456153.
[37] R. Sarkar, M. Boggio-Pasqua, P.-F. Loos, D. Jacquemin, *J. Chem. Theory Comput.*, **2021**, DOI:10.1021/acs.jctc.0c01228.
[38] Michael J. Frisch, G. W. Trucks, H. Bernhard Schlegel, Gustavo E. Scuseria, Michael A. Robb, James R. Cheeseman, Giovanni Scalmani, Vincenzo Barone, Benedetta Mennucci, G. A. Petersson, H. Nakatsuji, M. Caricato, Xiaosong Li, H. P. Hratchian, Artur F. Izmaylov, Julien Bloino, G. Zheng, J. L. Sonnenberg, M. Hada, M. Ehara, K. Toyota, R. Fukuda, J. Hasegawa, M. Ishida, T. Nakajima, Y. Honda, O. Kitao, H. Nakai, T. Vreven, J. A. Montgomery Jr., J. E. Peralta, François Ogliaro, Michael J. Bearpark, Jochen Heyd, E. N. Brothers, K. N. Kudin, V. N. Staroverov, Rika Kobayashi, J. Normand, Krishnan Raghavachari, Alistair P. Rendell, J. C. Burant, S. S. Iyengar, Jacopo Tomasi, M. Cossi, N. Rega, N. J. Millam, M. Klene, J. E. Knox, J. B. Cross, V. Bakken, C. Adamo, J. Jaramillo, R. Gomperts, R. E. Stratmann, O. Yazyev, A. J. Austin, R. Cammi, C. Pomelli, J. W. Ochterski, R. L. Martin, K. Morokuma, V. G. Zakrzewski, G. A. Voth, P. Salvador, J. J. Dannenberg, S. Dapprich, A. D. Daniels, Ö. Farkas, J. B. Foresman, J. V. Ortiz, J. Cioslowski, D. J. Fox, Gaussian 09, Revision E.01. Gaussian, Inc., 340 Quinnipiac St Bldg 40 Wallingford, CT 06492 USA, 2009.
[39] G. Hermann, V. Pohl, J. C. Tremblay, B. Paulus, H.-C. Hege, A. Schild, *Journal of Computational Chemistry*, **2016**, DOI:10.1002/jcc.24358.
[40] Y. Zhu, J. M. Herbert, *The Journal of Chemical Physics*, **2018**, DOI:10.1063/1.5004675.
[41] Y. Zhu, J. M. Herbert, *The Journal of Chemical Physics*, **2022**, DOI:10.1063/5.0079910.
[42] S. Klinkusch, J. C. Tremblay, *The Journal of Chemical Physics*, **2016**, DOI:10.1063/1.4948646.
[43] G. Hermann, J. C. Tremblay, *The Journal of Chemical Physics*, **2016**, DOI:10.1063/1.4966260.

[44] G. Füchsel, J. C. Tremblay, T. Klamroth, P. Saalfrank, *Israel Journal of Chemistry*, **2012**, DOI:10.1002/ijch.201100097.
[45] I. Tutunnikov, E. Gershnabel, S. Gold, I. Sh. Averbukh, *J. Phys. Chem. Lett.*, **2018**, DOI:10.1021/acs.jpclett.7b03416.
[46] I. Tutunnikov, J. Floß, E. Gershnabel, P. Brumer, I. Sh. Averbukh, A. A. Milner, V. Milner, *Phys. Rev. A*, **2020**, DOI:10.1103/PhysRevA.101.021403.
[47] A. Otero-de-la-Roza, E. R. Johnson, V. Luaña, *Computer Physics Communications*, **2014**, DOI:10.1016/j.cpc.2013.10.026.
[48] A. Otero-de-la-Roza, *The Journal of Chemical Physics*, **2022**, DOI:10.1063/5.0090232.
[49] S. R. Kirk, S. Jenkins, QuantVec. BEACON Research Group, College of Chemistry and Chemical Engineering, Hunan Normal University, Changsha, Hunan, P.R. China, 2021.
[50] S. R. Kirk, S. Jenkins, *WIREs Comput. Mol. Sci.*, **2022**, DOI:10.1002/wcms.1611.